BM@N Analysis Note
Study of charged hadron production in Xe+CsI collisions at E/A = 3.8 GeV.

Vadim Kolesnikov

June 2026

Abstract

In this note, the current status of the analysis of the production of $\pi^{\pm}, K^{\pm}$, and p in centrality-selected Xe+CsI collisions at E/A = 3.8 GeV (run8) is presented.

1 Introduction

Medium-mass nucleus-nucleus collisions at energies of several GeV per nucleon explore the high-density region of the QCD phase diagram. At intermediate energies, colliding nuclei can compress to densities exceeding normal nuclear matter, reproducing the conditions found inside neutron star mergers. The production of hadrons attracts attention for several reasons. Yields and ratios of different hadron species reveal the temperature and chemical equilibrium of the system. Using different combinations of beams and targets at BM@N, the initial neutron-to-proton ratio can be varied. Looking then at the ratio of charged pions π^-/π^+, the behavior of nuclear symmetry energy at supra-saturation densities and under different isospin asymmetry conditions can be unveiled. Kaons are the most sensitive diagnostic tools for measuring the strange sector of the nuclear matter Equation of State (EoS) and in-medium mass modifications. K^+-mesons experience a repulsive potential in a high-density baryon medium, in contrast to K^-, for which the in-medium potential is attractive. This shows up as distinct, measurable changes in the kaon transverse mass spectra. Measuring the rapidity distribution of protons reveals how much initial kinetic energy was lost during the collision. In addition, the ratio of produced light nuclei to protons allows testing cluster formation mechanisms and calculating the achieved entropy density and nucleon density fluctuations in the system.

The document is structured as follows. The next section describes the analysis procedure, including event and track selection criteria, particle identification, and corrections based on Monte Carlo detector simulations. The main results

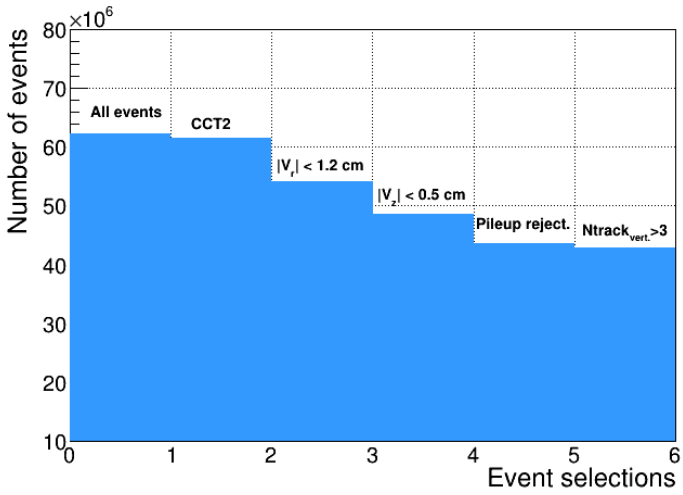


Figure 1: Number of Xe+CsI collisions satisfying the event selection criteria.

of this study are reported in Section 3, where the rapidity and centrality dependencies of particle yields and ratios are discussed in detail. The BM@N data are also compared to the DCM-SMM and UrQMD model predictions. The note concludes with a summary.

2 Data analysis

In this section, details of the data analysis procedure are presented. These include a description of the data set, event and track selection criteria, and particle identification. The corrections for the detector acceptance and efficiency were obtained from the BM@N simulation with the DCM-SMM model and GEANT package.

2.1 Data set

The data used in this analysis are Xe+CsI collisions collected by BM@N in 2023. The beam kinetic energy is 3.8 GeV per nucleon. The target width corresponds to 2% interaction probability. The Quality Assurance (QA) procedure is performed over the entire data sample to identify and eliminate bad runs. QA rely on the study run-by-run variations in the mean values of several quantities (mean track multiplicity, $\langle p_T \rangle$, DCA, etc). The information about bad runs was provided by A.Demanov. To ensure data quality during stable GEM performance, we used runs from 8002 to 8230 ($\approx 6.5 \cdot 10^7$ events in total). The estimated trigger cross-section for this period was approximately 80%.

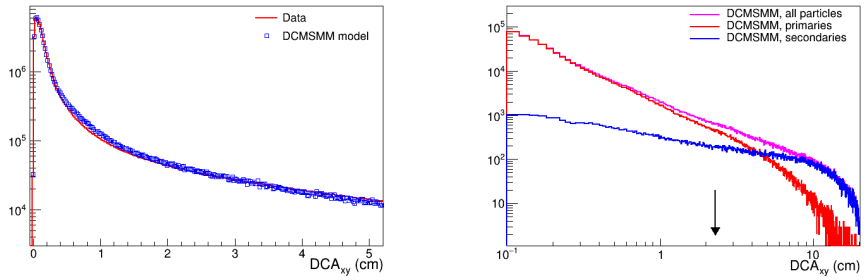


Figure 2: Left: DCA$_{xy}$ distributions in Xe+CsI collisions. Right: DCM-SMM model simulations of DCA$_{xy}$ for primary and secondary tracks in Xe+CsI collisions. The arrow indicates the applied selection cut.

2.2 Event selection

The analysis starts with the selection of events using the CCT2 trigger, which requires a coincidence of signals from the beam counters and the Barrel Detector ($N_BD_Hits > 3$), combined with an anti-coincidence from the Fragment Detector (FD). For this analysis, events with the primary vertex z-position within ± 0.5 cm of the nominal target position were selected. Furthermore, a radial distance cut of $|V_r| < 1.2$ cm was applied, where V_r represents the distance between the collision vertex and the target center in the transverse plane. The recorded amplitude in the FD was required to be below the value for the beam particle (FD$_{ampl} < 4250$).

If more than one collision occurs within the BM@N read-out time interval, two or more events can be reconstructed as a single event, leading to pile-up. These pile-up events with unusually high event multiplicity must be rejected. The pile-up removal procedure, which was developed by V.Plotnikov and L.Kovachev, relies on the integral of the Beam Counter 2 (BC2) signal within a predefined time window (BC2$_{integr} < 11000$) and the presence of TOF hits in a time interval outside the main trigger time window. To ensure high-quality vertex and track reconstruction, only events with more than three tracks assigned to the primary vertex were selected.

After all the event selection criteria were applied, $4.2 \cdot 10^7$ valid events were retained for the subsequent analysis (see Fig. 1).

2.3 Track selection

In this analysis, we used global tracks that are attached to the main vertex and have a TOF hit. The entire sample of reconstructed tracks contains a fraction of tracks from hyperon decays and secondary interactions. After extrapolation to the interaction point, these tracks exhibit a wider distribution of the Distance of Closest Approach (DCA) value than that of primary tracks. Thus, a DCA cut can be employed to ensure a high purity of primary parti-

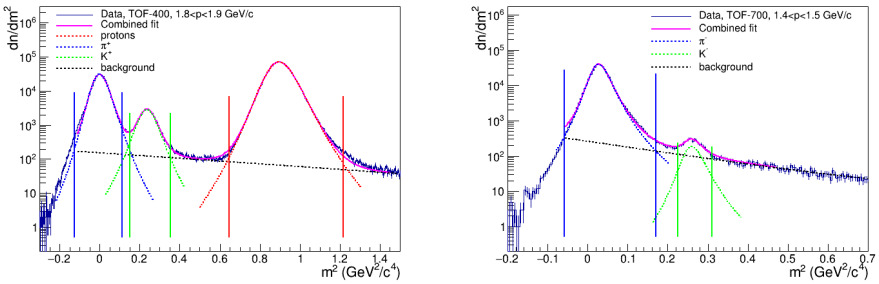


Figure 3: m^2 distribution for positively charged (left panel) and negatively charged (right panel) hadrons from Xe+CsI collisions. The colored dashed lines indicate the contributions of individual particle species to the total fit (shown by the solid purple line). The solid colored vertical lines indicate the selection windows.

cles. The optimal value of this cut was obtained from the simulation of the BM@N setup with the DCM-SMM model. We used $2.0 \cdot 10^5$ simulated Xe+CsI collisions with an impact parameter cut of $b < 11.5$ fm, which corresponds to the experimental data centrality interval of 0-80%. The simulated events were processed using the same analysis chain as the experimental data. First, we compared the DCA distribution in the transverse plane, DCA_{xy}, in the experimental data and the model simulation (see the left panel in Fig. 2). Here $\mathrm{DCA}_{xy} = \sqrt{DCA_x^2 + DCA_y^2}$. The data and the model show reasonable agreement. Second, based on the DCM-SMM distributions of the DCA_{xy} value for primary and secondary tracks (see Fig. 2, right panel), the DCA cut value was chosen such that the remaining fraction of secondaries was approximately equal to the loss of primary tracks. The resulting optimal cut value was found to be $\mathrm{DCA}_{xy} = 2.3$ cm.

We also required each track to have at least 4 hits in the BM@N tracker (nHits>3). Furthermore, track momenta were restricted to $p > 0.4$ GeV/c and $p_T > 0.1$ GeV/c.

2.4 Particle identification

At BM@N, the mass-squared from the TOF-400 and TOF-700 systems is used for particle identification. The m^2 quantity is derived as follows:

$$m^2 = p^2 \left(\frac{c^2 t^2}{l^2} - 1 \right), \tag{1}$$

where p is the particle's total momentum, l is the path length, and t is the time of flight. Mass-squared distributions were analyzed in the total momentum bins of 100 MeV/c. As an example, the left panel in Fig. 3 shows the m^2 distributions for positively charged particles in the momentum range of $1.8 < p < 1.9$ GeV/c

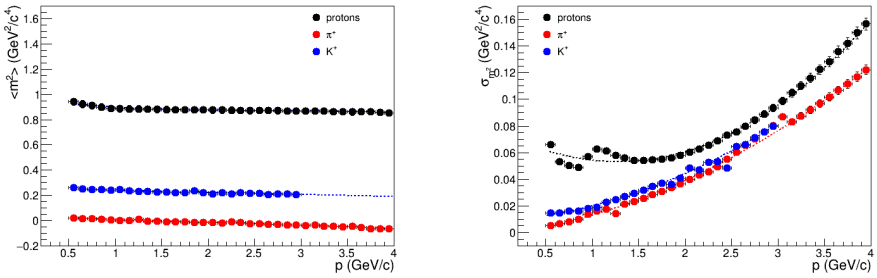


Figure 4: Momentum dependence of $\langle m^2 \rangle$ and σ_{m^2} for positively charged hadrons measured in the TOF-400 detector. The dashed lines indicate the parameterization results.

from the TOF-400 detector. The right panel shows the distribution for negatively charged particles from the TOF-700 system.

It was found that none of the signal peaks could be satisfactorily described by a Gaussian distribution due to their heavy tails and rightward asymmetry. Thus, the m^2 distribution in each momentum bin was modeled by a combination of skewed Student's t-distributions and a background contribution described by the sum of an exponential and a polynomial function. The StudentPdf function (TMath::StudentPdf($m^2, parameters$)) has five parameters: the amplitude A, the mean $\langle m^2 \rangle$, the width σ, the number of degrees of freedom $ndof$ (which determines the peak tail behavior), and the skewness parameter ν. The pion, kaon and proton peaks maintain similar shapes across different centrality intervals. Figure 4 shows the momentum dependence of $\langle m^2 \rangle$ (left panel) and σ (right panel) for π^+, K^+, and p. If a free fit parameter deviated by more than 3σ from the predefined momentum dependence (see the dashed lines in Fig. 4), the fit procedure was repeated with that parameter fixed to the value obtained from the parameterization function. The $ndof$ and ν parameters of pions and kaons are fixed to the corresponding parameters of the proton peak.

The raw particle yields are obtained by counting the number of tracks within the predefined selection windows (see the vertical colored lines in Fig. 3). The PID corrections for particles lying outside the selection window, as well as for the background contamination within the signal window were estimated by integrating the signal and background functions over the respective m^2 ranges.

2.5 Collision centrality definition

In nucleus-nucleus interactions, the concept of collision centrality is directly related to the impact parameter b, defined as the distance between the centers of the colliding nuclei. Central collisions feature a small b and a large overlap region, whereas peripheral collisions are characterized by a large impact parameter where only a few nucleons participate. Since particle production is predominantly driven by nucleon-nucleon interactions within the overlap zone,

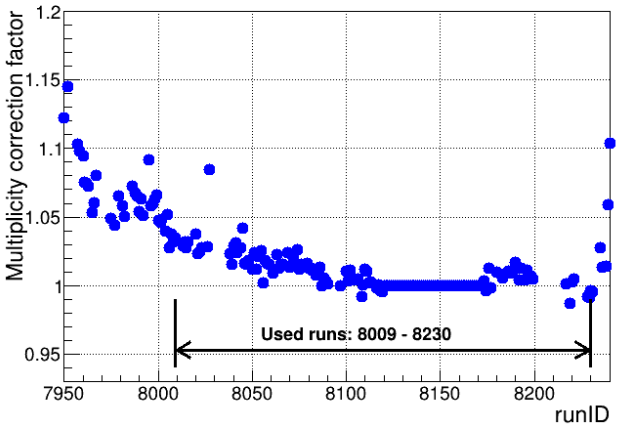


Figure 5: Run dependence of the $refMult$ correction factors. The arrow indicates the range of the analyzed runs.

track multiplicity serves as a reliable proxy for collision centrality. In this analysis, centrality was defined using the multiplicity of global tracks (N_{glob}). This quantity, however, is sensitive to the BM@N tracking efficiency, which fluctuated throughout the 2023 data-taking period. To ensure a uniform multiplicity distribution across the entire data set, these fluctuations were compensated for by scaling N_{glob} on a run-by-run basis. The correction procedure was developed by A.Demanov. First, a baseline multiplicity distribution was obtained using a subset of runs (8120–8170). Then, the correction factor for a given run was calculated as the ratio of its high-end multiplicity distribution point to that of the baseline distribution. The resulting run dependence of these scaling factors is presented in Figure 5, where the corrected track multiplicity is denoted as the reference multiplicity $refMult$. For the analyzed run range, the maximum deviation of $refMult$ from the baseline remains below 5%.

Figure 6 presents the area-normalized $refMult$ distributions (pdf) for the pileup-rejected data (red line) and the DCM-SMM model. The experimental $refMult$ value was scaled up by 4% to better reproduce the shape of the model's pdf in the mid- and high-end regions of the distribution. Furthermore, the distributions were normalized by the ratio of their integrals in the range of $refMult = [60, 200]$. The resulting distributions agree well in central and mid-central collisions, except for the region of $refMult > 210$, where residual pileup contribute to the data. In contrast, the discrepancy between the data and the model at low $refMult$ values arises from a drop in trigger efficiency for peripheral collisions. Centrality intervals, indicated by the vertical lines in Fig. 6, are determined from the respective fractions of the total integral of the model distribution. Table 1 lists the selected centrality classes along with the corresponding $refMult$ boundaries. The indicated impact parameter intervals and

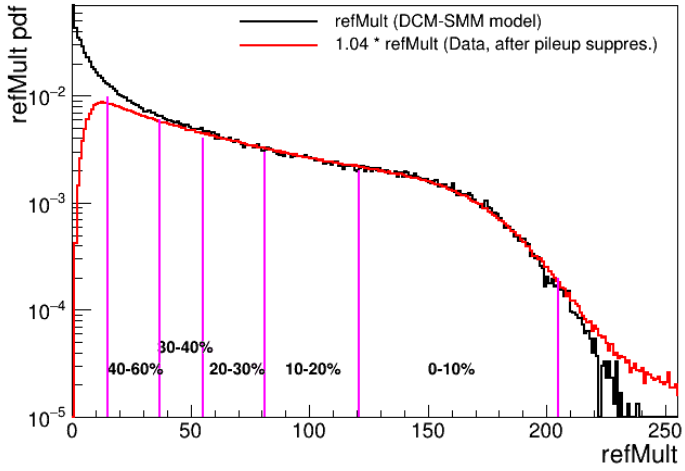


Figure 6: Area-normalized $refMult$ distributions for Xe+CsI collisions at $E_{beam} = 3.8$A GeV. The vertical lines indicate the centrality boundaries.

the mean number of participants ($\langle N_{part} \rangle$) were both derived from a Glauber model.

Table 1: Centrality intervals and the corresponding $refMult$ ranges for the BM@N 2023 data set. The impact parameter intervals and mean numbers of participants are derived from a Glauber model.

Centrality class (%)	$refMult$ min.	$refMult$ max.	$b_{min} - b_{max}$	$\langle N_{part} \rangle$
0–10	121	193	0–4	200
10–20	81	121	4–5.7	143
20–30	55	81	5.7–7.0	100
30–40	37	55	7.0–8.1	68
40–60	15	37	8.1–9.9	36

2.6 Corrections

Raw particle spectra need to be corrected for the finite detector acceptance, efficiency, and losses from selection criteria and particle identification. The correction factor, which includes the TOF acceptance, tracking efficiency, and losses during particle propagation in the BM@N material, was obtained from Monte-Carlo simulations with the DCM-SMM model. We used the reconstructed model data from:
/eos/nica/bmn/sim/dst/DCMSMM/DCMSMMmod_XeCsI_3.8AGeV_mb_2.5k/
The correction factor ϵ_{acc} was defined as the ratio of the number of particles of

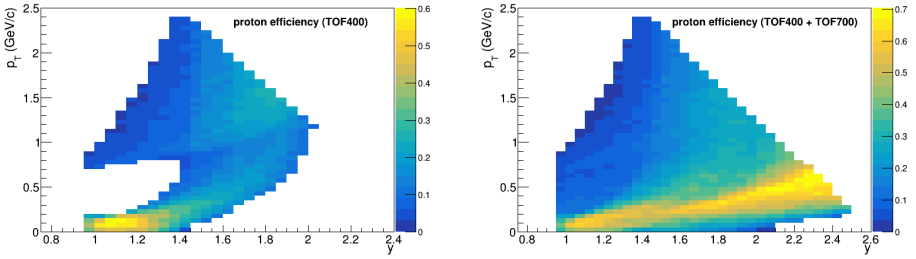


Figure 7: BM@N acceptance for protons in the TOF-400 system (left) and the TOF-400/TOF-700 combination (right).

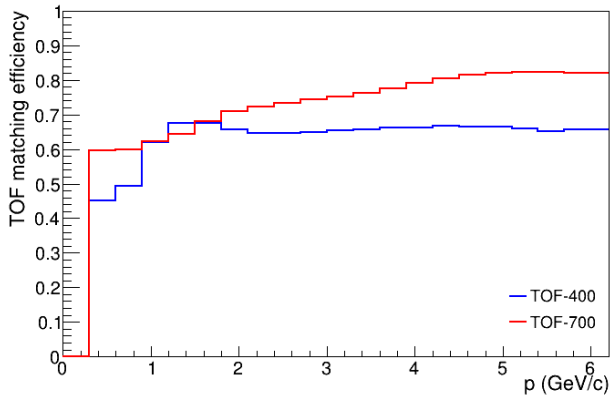


Figure 8: The momentum dependence of ϵ_{TOF} in the TOF-400 and TOF-700 detectors.

a particular species with a TOF hit that passed all selection criteria (number of hits, DCA, etc.) to the number of generated particles in the same phase-space bin. Figure 7 presents the two-dimensional distribution of ϵ_{acc} for protons as a function of p_T and rapidity for the TOF-400 system (left panel) and the combined TOF-400/TOF-700 detectors (right panel).

The TOF efficiency ϵ_{TOF}, which includes the TOF matching efficiency and the overall operational efficiency (i.e of non-working strips and fluctuation in the TOF performance during data taking) was obtained using a data-driven method. For this purpose, all global tracks in an event were extrapolated from their last measured point to the TOF detector plane. ϵ_{TOF} was then defined as the ratio of the number of the registered TOF hits to the total number of extrapolated tracks. The momentum dependence of ϵ_{TOF} is shown in Fig. 8 for the TOF-400 (blue line) and TOF-700 (red line).

The reconstructed spectra of pions and protons contain secondary $\pi^{\pm}, p$ from the decays of hyperons and K^0_S mesons. Although an estimate based on the

DCM-SMM model indicates a 1–2% contamination, no correction was applied in the present analysis.

2.7 Systematic uncertainties

The systematic uncertainties in the invariant yields of identified hadrons were evaluated by tightening or loosening the analysis criteria around their nominal values. The varying parameters include the primary vertex z-position and V_r windows, the track DCA cut to the primary vertex, and the PID selection windows. The total systematic uncertainty contributed by event/track selection and PID signal extraction is about 3%.

The systematic uncertainty associated with the detector acceptance, tracking, and TOF matching efficiency corrections is evaluated by varying the track and TOF matching quality selection criteria (minimum number of hits, χ^2/ndf, ΔX and ΔY of the track-TOF matching) simultaneously in both the experimental and the Monte Carlo data. In addition, the difference in the correction table obtained with two distinct input distributions for the detector simulation, namely, the DCM-SMM model (providing a realistic track multiplicity environment, but having low p_T–y bin statistics) and a flat box distribution (providing high bin-by-bin statistics with a less realistic phase-space distribution), was used to estimate the overall uncertainty due to these corrections.

The overall systematic uncertainty of the hadron yields in individual phase-space bins is estimated to be approximately 6%. An additional systematic uncertainty of 2% was assigned to pions and protons due to contamination from weak decay feed-down (from hyperons and K^0_S).

In estimating the scaling behavior of particle yields, an additional uncertainty of 5% in the $\langle N_{part}\rangle$ value was introduced. This number was estimated as the difference between the $\langle N_{part}\rangle$ predictions from the UrQMD and the Glauber model.

Moreover, the uncertainty in the particle yields obtained via extrapolations into the unmeasured phase-space regions, wich affects the rapidity density dn/dy and the total multiplicity $\langle n\rangle$, is discussed in Section 3.

3 Results

In this section, the main results of the analysis are reported. In subsection 3.1, the invariant p_T spectra of $\pi^{\pm}, K^{\pm}$, and p are presented. Subsection 3.2 presents the rapidity spectra of the hadrons, their total multiplicities, and the scaled particle ratios. A comparison of the BM@N measurements with the model predictions for dn/dy in centrality-selected Xe+CsI events is also discussed.

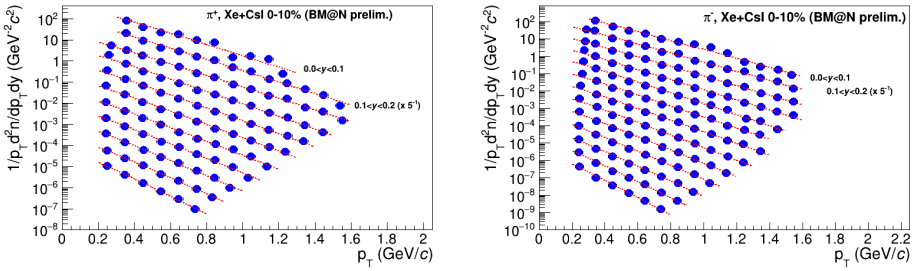


Figure 9: Invariant p_T spectra of π^+ (left) and π^- (right) in the 0–10% most central Xe+CsI collisions. The red dashed lines indicate the fits to the thermal function.

3.1 Transverse momentum spectra of $\pi^{+/-}$, $K^{\pm}$, and p in centrality-selected Xe+CsI collisions.

Figure 9 shows the final invariant transverse momentum spectra of π^+ (left panel) and π^- (right panel) in the 0–10% most central Xe+CsI collisions. The spectra were obtained in 0.1-wide rapidity bins and scaled down by successive powers of 5 for clarity. To fit these spectra, we used a thermal function defined as

$$\frac{1}{p_T}\frac{d^2n}{dp_T dy} = const \cdot \exp\left(-\frac{m_T - m}{T}\right), \tag{2}$$

where $m_T = \sqrt{p_T^2 + m^2}$ and T is the slope parameter (effective temperature). The resulting fits are shown in the figure as dashed lines.

It is known that pion transverse spectra in nucleus-nucleus collisions are enhanced at low p_T due to feed-down from resonance decays (Δ, N^*, ρ, ω) and in-medium interactions. This enhancement over the simple exponential trend increases with collision centrality and towards midrapidity. Usually, a sum of two exponential functions is used to describe pion spectra. However, the lack of the BM@N acceptance for pions at $p_T < 200$ MeV/c prevents an accurate estimation of the difference in the extrapolation between single- and double-exponential functions. A rough estimate of the uncertainty due to the choice of the pion spectrum shape at low p_T was performed by fitting the p_T distributions near midrapidity with a double-exponential function where the slope parameter at low transverse momentum was fixed to a value taken from the literature ($T_{low} \approx 60$ MeV). The difference between the calculated total yields per unit of rapidity (dn/dy) for these two approaches is about 12% and 15% for π^+ and π^-, respectively. It was taken as an additional systematic uncertainty for the dn/dy of pions (see subsection 3.2).

The invariant p_T spectra of charged kaons in the 0–10% most central Xe+CsI collisions are shown in Fig. 10. As in the case of pions, the thermal function in Eq. 2 was used to fit the spectra (see the red dashed lines).

Figure 11 presents the final invariant transverse momentum spectra of pro-

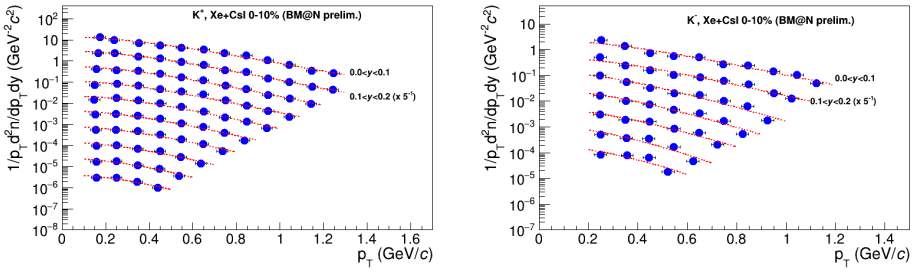


Figure 10: Invariant p_T spectra of K^+ (left) and K^- (right) in the 0–10% most central Xe+CsI collisions. The red dashed lines indicate the fits to the thermal function.

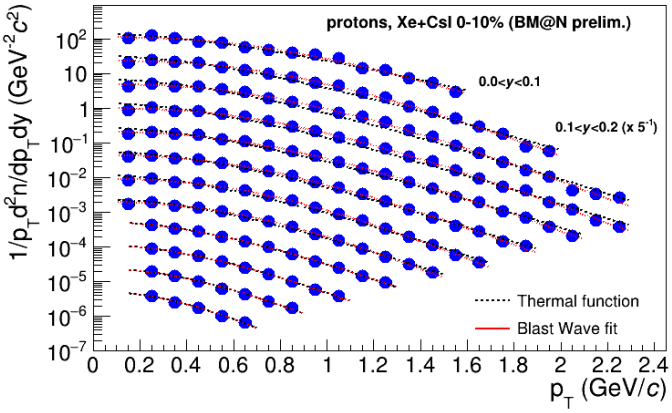


Figure 11: Invariant p_T spectra of protons in the 0–10% most central Xe+CsI collisions. The black and red dashed lines indicate the fits to the thermal and the Blast-Wave function, respectively.

tons in the 0-10% most central Xe+CsI collisions. We utilize two functional forms to fit the spectra of protons across varying rapidity and collision centrality intervals: a thermal function (see the black dashed lines in Fig. 11), and a Blast-Wave-motivated function (see the read lines in Fig. 11), defined as follows

$$\frac{d^2N}{p_T dp_T dy} \propto \int_0^R r\, dr\, m_T K_1\left(\frac{m_T \cosh\rho}{T_{fo}}\right) I_0\left(\frac{p_T \sinh\rho}{T_{fo}}\right), \tag{3}$$

where $\rho = \tanh^{-1}(\beta_T)$, $\beta_T(r) = \beta_s\,(r/R)^n$. Here T_{fo}, β_s, and n are the fit parameters. It was found that the Blast-Wave (BW) function describes the shape of the midrapidity spectra significantly better than the thermal function; therefore, the results of BW fits were used to extrapolate the proton spectra into unmeasured p_T regions (see next subsection).

Since the purely thermal Boltzmann distribution does not satisfactorily describe the shape of the p_T spectra of heavy particles, and the slope parameter T depends on the p_T range used in the fitting procedure, we utilize the mean transverse momentum $\langle p_T \rangle$ to characterize the shape. The $\langle p_T \rangle$ of the proton spectra is shown in Fig. 12 (left panel) as a function of the center-of-mass rapidity. For a particular distribution, $\langle p_T \rangle$ is given as the mean of the BW fit function within $p_T = [0, 3]$ GeV/c, with the uncertainty estimated using the bootstrap method. In the expanding fireball, the mean transverse momentum of hadrons results from a combination of their thermal motion and the contribution from radial expansion in the collective velocity field. In matter under thermal equilibrium, the former contribution is equal for all hadron species, while the latter is proportional to particle mass:

$$\langle p_T \rangle \approx \langle p_T \rangle_{thermal} + m\langle \beta_T \rangle \tag{4}$$

As shown in Fig. 12, the distribution peaks in the midrapidity region for all centralities, indicating that this is the hottest zone of the fireball with the largest radial expansion. The point closest to midrapidity deviates from the common trend indicated by the parabolic fit functions (dashed lines); therefore, the extrapolated value of the fit function was taken as the final midrapidity $\langle p_T \rangle$. The right panel of Fig. 12 shows the mass dependence of the midrapidity $\langle p_T \rangle$ for π^+, K^+, and p in 0–10%, 20–30%, and 40–60% central collisions. The observed linear scaling of $\langle p_T \rangle$ with particle mass is a characteristic signature of a collective radial expansion in the created matter. To examine how this mass dependence varies with collision centrality, the data points are scaled to the pion $\langle p_T \rangle$ value in the most peripheral centrality bin. As can be seen from the figure, the rate of change of $\langle p_T \rangle$ increases modestly towards more central collisions (dashed lines indicate linear fits serving as a guide to the eye). Furthermore, to quantify the thermodynamic fireball parameters, we study the results of the BW fits, which, in addition to providing a reliable extrapolation to the unmeasured p_T ranges, allow the average radial flow velocity $\langle \beta_T \rangle$ and the kinetic freezeout temperature T_{fo} to be extracted.

An example of the BW fit to the combined p_T spectra of π^+, K^+, and p is shown in Fig. 13. The data points are represented by solid symbols, while the BW fit results are depicted by solid lines.

Figures 14 and 15 demonstrate the rapidity dependence of $\langle \beta_T \rangle$ and T_{fo}, respectively, for various centrality classes in Xe+CsI collisions. These parameters were obtained from the BW fits to combined $\pi/K/p$ spectra (red symbols), and compared to those obtained from the individual proton spectra (as exemplified for 0–10% central collisions in Fig. 11). As illustrated, $\langle \beta_T \rangle$ reaches a maximum at midrapidity and steadily decreases toward the beam rapidity. This behavior reflects the fact that radial expansion is driven by the local initial pressure gradient in the interaction zone, which naturally peaks at midrapidity and falls off toward the fragmentation regions. Furthermore, the radial flow velocity in central collisions extracted from the individual proton fits is systematically larger than that obtained from the combined fits. Due to their relatively large

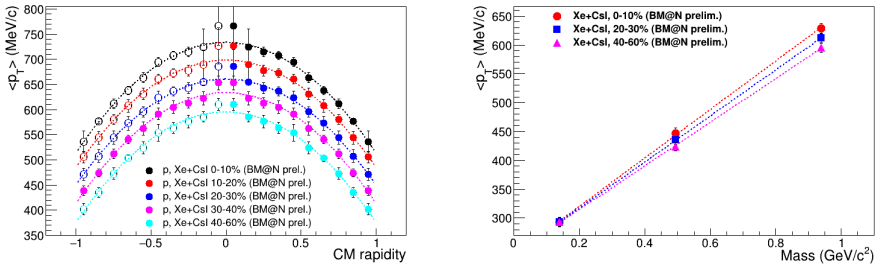


Figure 12: Left: $\langle p_T \rangle$ of protons in centrality-selected Xe+CsI collisions as a function of the center-of-mass rapidity. Right: $\langle p_T \rangle$ for π^+, K^+, p in 0–10%, 20–30%, and 40–60% central collisions.

mass, protons receive a strong momentum boost from the collective expansion, leading to a pronounced flattening of their spectra at low-to-mid p_T. When protons are fitted independently – lacking the tight constraints imposed by light hadron spectra – the minimizer drives $\langle \beta_T \rangle$ to higher values to accommodate this spectral hardening. From the other hand, the curves for $\langle \beta_T \rangle$ obtained from both the individual proton fits and the combined fits exhibit a roughly parallel behavior across the entire investigated rapidity range, suggesting that the systematic differences between the two fitting methods are independent of longitudinal dynamics.

Regarding the kinetic freeze-out temperature, the opposite trend is observed: in central collisions the combined fit yields a systematically larger temperature compared to the individual proton fits. This behavior is a direct consequence of the strong mathematical anti-correlation between T_{fo} and $\langle \beta_T \rangle$ inherent to the Blast-Wave parametrization. In contrast to radial velocity T_{fo} does not demonstrate a definite trend across rapidity. Except for the most central interval, temperature varies slowly over a large rapidity range. This flat trend suggests that the local kinetic freeze-out is triggered when the system's local energy or particle density drops below a universal critical threshold, which remains relatively uniform across the longitudinal expansion zone.

The values of $\langle \beta_T \rangle$ and T_{fo} for the combined BW fits, averaged over the rapidity interval $y = [0, 0.5]$, are 0.43 ± 0.01 and 89 ± 6 MeV, respectively, in the 0–10% most central Xe+CsI collisions. These results are in reasonable agreement with the STAR measurements for 0-5% central Au+Au reactions at $\sqrt{s_{NN}} = 3.2$ GeV: $\langle \beta_T \rangle \approx 0.42 \pm 0.02$ and $T_{fo} \approx 85 \pm 3$ MeV (see the STAR report on charged hadrons at SQM'26).

3.2 Rapidity distributions of hadrons, particle ratios, and comparison with model predictions

The rapidity density dn/dy of hadrons was calculated as the sum of the integrated yield over the measured p_T range and the contribution from the ex-

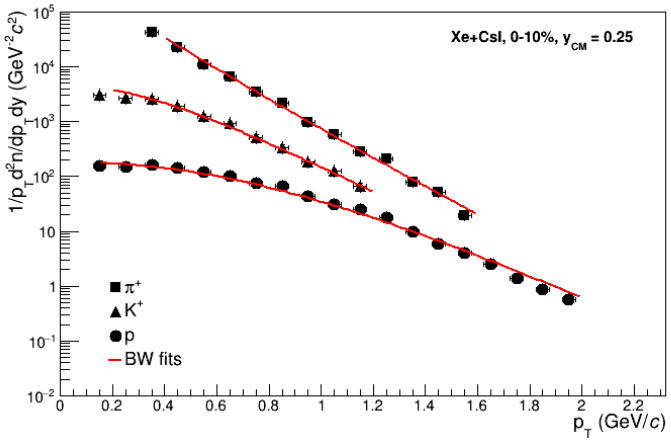


Figure 13: Combined Blast-Wave fit (solid lines) to the invariant p_T spectra of π^+, K^+, and p (solid symbols).

trapolation into unmeasured regions. This extrapolation contributes 30%–50%, 10%–35%, and 3%–30% of the total yield for $\pi^{\pm}$, $K^{\pm}$, and p, respectively, depending on the actual p_T coverage. To quantify the systematic uncertainty due to the missing p_T coverage, the spectral extrapolation was performed using different fit functions (e.g., single-, double-exponential, BW). The maximum deviation between the extracted yields was taken as an additional systematic uncertainty on the dn/dy values. Figures 16–20 show rapidity distributions of $\pi^{\pm}, K^{\pm}$, and p in centrality-selected Xe+CsI collisions. The measurements are shown by the solid symbols, while the open symbols represent data points reflected about midrapidity. The error bars indicate statistical uncertainties, while the systematic uncertainties are shown by the open rectangles. The colored lines represent the predictions of the UrQMD and DCM-SMM models. *Note: The procedure of event centrality selection for the DCM-SMM model was performed using the same refMult windows as in the data, because the reconstructed events for this model have the same format as the experimental data. The centrality windows for the UrQMD model were defined using the impact parameter values listed in Table 1.*

The agreement between the experimental results for charged pions and the model predictions is reasonable in all centrality intervals, except in the midrapidity region where the difference reaches 8–15% (with the DCM-SMM model showing better agreement).

The measurements for K^+ are very well reproduced by the DCM-SMM model, while the UrQMD model predictions lie 15–20% above the data. However, both models underpredict the yields of negatively charged kaons.

The shape of the rapidity distributions of protons in mid-central and peripheral collisions is well described by the models, except in the fragmentation region

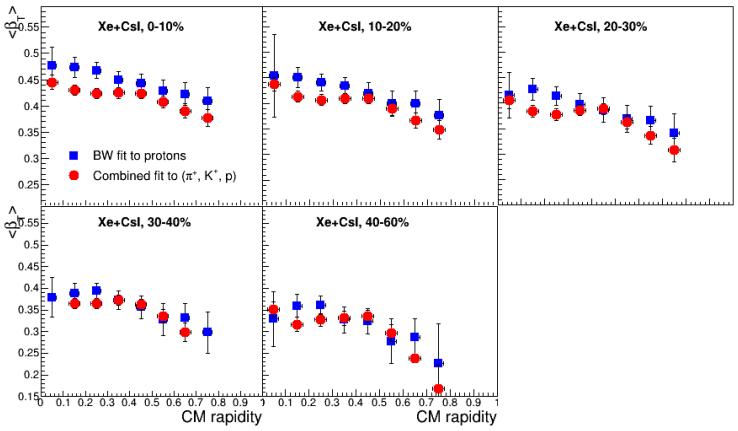


Figure 14: Average radial expansion velocity as a function of the center-of-mass rapidity in centrality-selected Xe+CsI collisions. The data points are obtained from the BW fits to the proton p_T spectra and to the combined $\pi/K/p$ spectra.

where the DCM-SMM model predicts a 50% larger yield. In central collisions, the data exhibit a larger degree of stopping, exceeding the model predictions at midrapidity by 15% in the 0–10% most central collisions.

The total multiplicity of a given meson, $\langle n \rangle$, was calculated by summing the integrated yields from all rapidity bins, assuming that the data points reflected about midrapidity represent real measurements, and adding the extrapolated yield over the unmeasured rapidity ranges. The extrapolation was determined as the integral of the fit function over the unmeasured rapidity region. It is known that the double-Gaussian function describes the tails of the meson rapidity distributions better than the single Gaussian one. Therefore, we used this functional form for the extrapolation. The uncertainty of the total yield was taken as the difference between the $\langle n \rangle$ values obtained with double- and single-Gaussian fits. This extrapolation contributes about 20–25% to the total yield. Figure 21 (left panel) shows the total multiplicity of π^+ scaled by the mean number of participants as a function of $\langle N_{part} \rangle$. The results of this analysis are compared to the earlier BM@N measurements from Ar+A reactions at lower collision energies [1]. The scaled pion multiplicity in Xe+CsI is flat over a wide centrality range and lies slightly above the Ar+A data (as expected for collisions of heavier systems at higher energies). *Note : The average number of participants for the Ar+A data was calculated within the Glauber approach, assuming a 0–80% trigger cross section for all reactions.*

Pion production at Nuclotron energies is dominated by the excitation and subsequent decay of $\Delta(1232)$ resonances. The final π^-/π^+ ratio is dictated by the initial neutron-to-proton (N/Z) ratio in the overlapping zone (overall $N/Z = 1.35$ in Xe+CsI) and the collision rate in the dense baryonic medium, which enables the transfer of initial isospin imbalance from nucleons to pions.

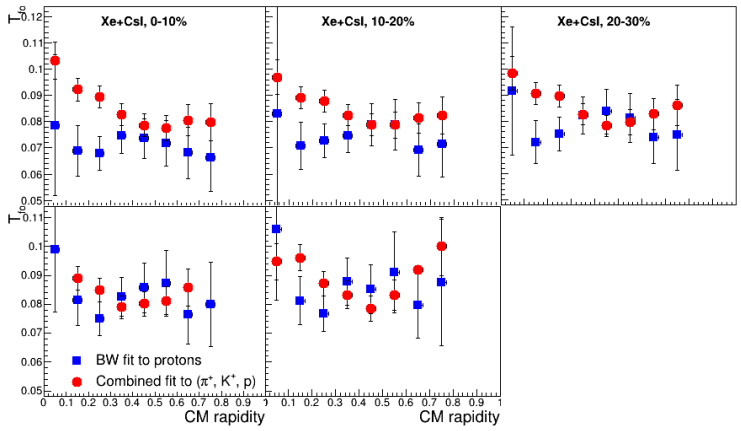


Figure 15: Kinetic freezeout temperature as a function of the center-of-mass rapidity in centrality-selected Xe+CsI collisions. The data points are obtained from the BW fits to the proton p_T spectra and to the combined $\pi/K/p$ spectra

Therefore, one might expect that a higher density and a larger number of multiple binary collisions in central events would alter the production rates of pions making the π^-/π^+ ratio larger in more central collisions. On the other hand, if the neutron skin effect is indeed present in medium-size nuclei such as xenon, the initial N/Z ratio could increase from central to peripheral collisions. The right panel of Fig. 21 shows the centrality dependence of the midrapidity π^-/π^+ ratio in Xe+CsI collisions. The colored dashed lines depict the corresponding model predictions for this ratio. As shown, based on the uncertainties of the present data points, one might not draw definitive conclusions about a potential centrality dependence of the ratio.

The yields of $\pi^\pm$ scale linearly with $\langle N_{part}\rangle$ at Nuclotron energies, while the multiplicity of strange hadrons per participating nucleon grows with collision centrality more rapidly: $\langle n\rangle \propto N_{part}^{\alpha_S}$, where $\alpha_S > 1$ [2, 3]. This behavior is explained by the effect of dynamical energy accumulation through sequential multi-step hadronic rescattering in the dense baryonic medium, mainly via the excitation of short-lived baryonic resonances which can then undergo secondary interactions. Since the probability of such secondary multi-step processes scales with the local baryon density, this energy accumulation effect becomes remarkably efficient in central collisions, enabling production of strange and multi-strange hadrons even below the free nucleon-nucleon NN kinematics threshold. It is therefore interesting to investigate this energy accumulation effect at BM@N within intermediate-size systems using the available data on charged kaons.

The right panel of Fig. 22 shows the total multiplicity of $K^\pm$ per participating nucleon as a function of $\langle N_{part}\rangle$ for Xe+CsI collisions. The normalized yields exhibit a monotonic increase with centrality, while keeping the K^+/K^- ratio flat. Fitting the data with a power-law function returns $\alpha_S = 1.20 \pm 0.11$ and

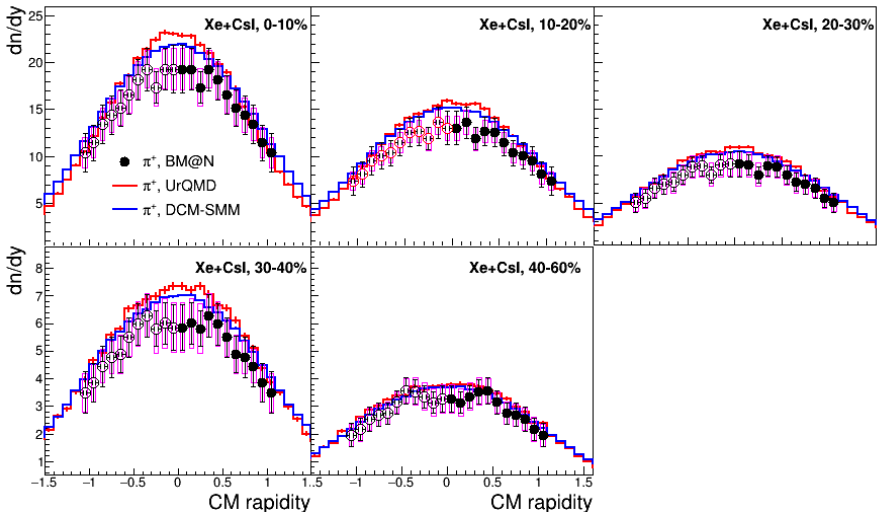


Figure 16: Rapidity distributions of π^+ in centrality-selected Xe+CsI collisions. Solid symbols show the experimental measurements, while open symbols represent data points reflected about midrapidity. The error bars indicate statistical uncertainties, while the systematic uncertainties are shown by the open rectangles. The UrQMD and DCM-SMM model predictions are represented by the red and blue lines, respectively.

$\alpha_S = 1.21 \pm 0.12$ for K^+ and K^-, respectively. The α_S parameter in Xe+CsI collisions is smaller than the values reported by the HADES and STAR collaborations for more massive Au+Au collisions [2, 3] (see the left panel of Fig. 22). The question whether the observed universality for the scaling parameter for strange hadrons persists in Xe+CsI will be addressed when the final BM@N data on K^0_S and Λ become available.

4 Summary

This note presents the current status of the analysis of charged production ($\pi^{\pm}, K^{\pm}$, and p) in centrality-selected Xe+CsI collisions. An overview of the analysis procedure, including event and track selection criteria, particle identification, and corrections based on Monte Carlo detector simulations is given. The invariant p_T spectra of charged pions, kaons, and protons were obtained for various centrality classes in several rapidity bins. The shapes of these spectra were analyzed within the framework of the Blast-Wave model. The values of the average radial velocity and the kinetic freezeout temperature were obtained as a function of rapidity for different centrality intervals. The measured hadron rapidity spectra were compared with predictions from the UrQMD and DCM-SMM models. The $\langle N_{part} \rangle$ scaling behavior of the total multiplicities and

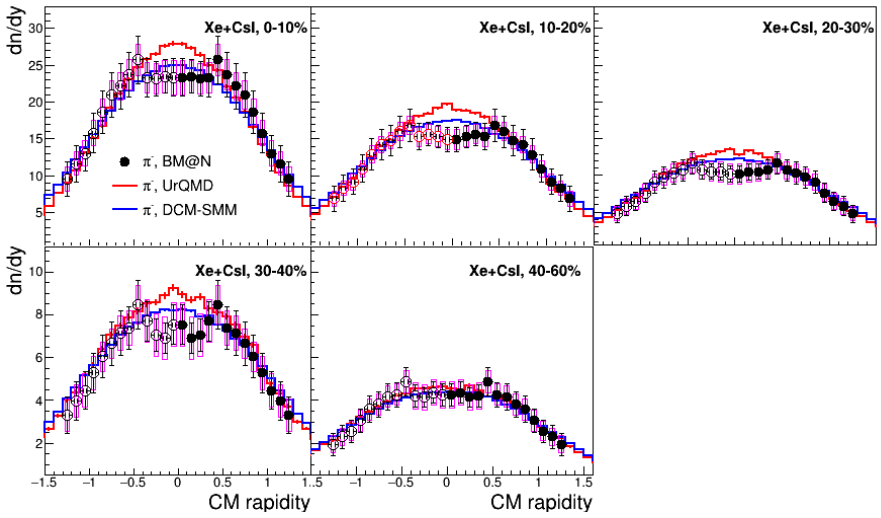


Figure 17: The measured rapidity spectra of π^- in centrality-selected Xe+CsI collisions (black circles). The error bars indicate statistical uncertainties, while the systematic uncertainties are shown by the open rectangles. The UrQMD and DCM-SMM model predictions are shown by the red and blue lines, respectively.

particle ratios was also investigated.

References

[1] S. Afanasiev et al. (BM@N Collab.), JHEP **2307**, 174 (2023); arXiv: 2303.16243.

[2] HADES Collaboration, Phys. Lett. B 793 (2019) 457.

[3] STAR Collaboration 2407.10110v1 [nucl-ex] 14 Jul 2024.

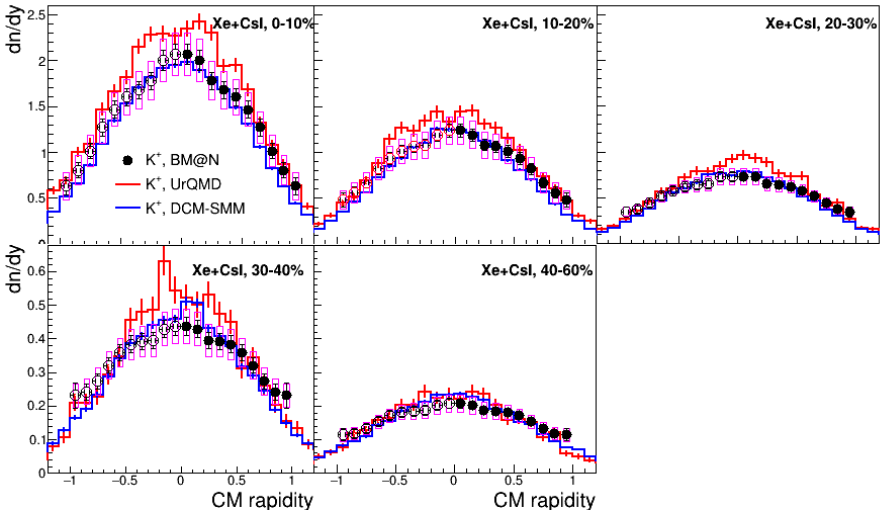


Figure 18: The measured rapidity spectra of K^+ in centrality-selected Xe+CsI collisions (black circles). The UrQMD and DCM-SMM model predictions are represented by the red and blue lines, respectively.

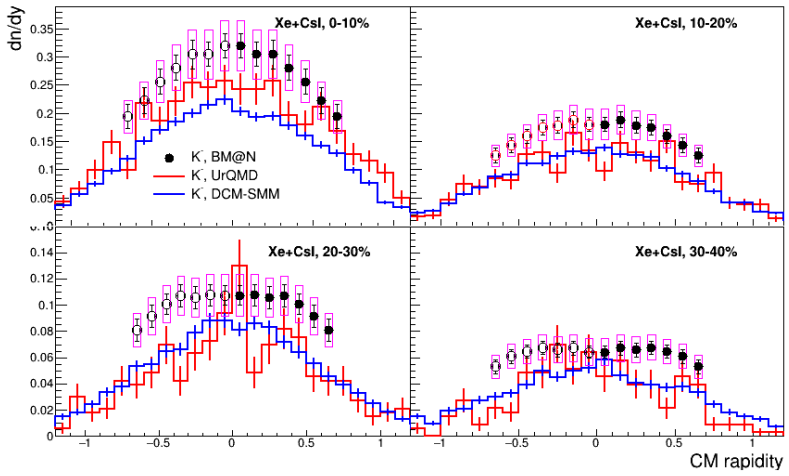


Figure 19: The measured rapidity spectra of K^- in centrality-selected Xe+CsI collisions (black circles). The error bars indicate statistical uncertainties, while the systematic uncertainties are shown by the open rectangles. The UrQMD and DCM-SMM model predictions are represented by the red and blue lines, respectively.

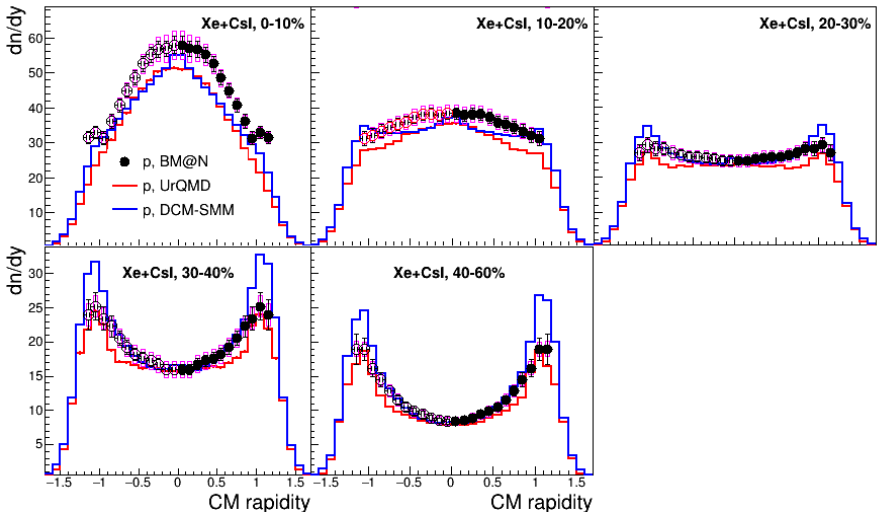


Figure 20: The measured rapidity spectra of protons in centrality-selected Xe+CsI collisions (black circles). The error bars indicate statistical uncertainties, while the systematic uncertainties are shown by the open rectangles. The UrQMD and DCM-SMM model predictions are represented by the red and blue lines, respectively.

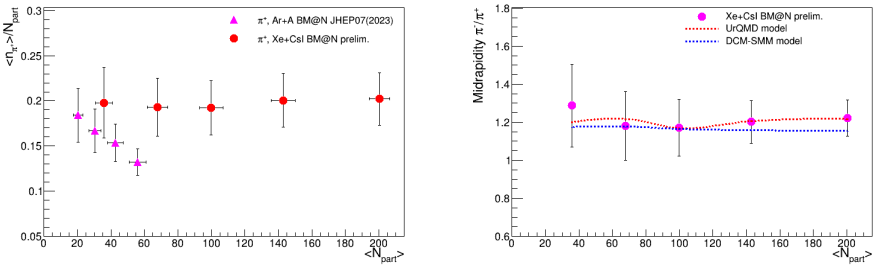


Figure 21: Left: The total multiplicity of π^+ scaled by the mean number of participants as a function of $\langle N_{part} \rangle$. The Xe+CsI results are from this analysis, while the Ar+A data are taken from Ref. [1]. Right: The centrality dependence of the midrapidity π^-/π^+ ratio in Xe+CsI collisions. The BM@N data are shown by the solid symbols, while the colored dashed lines depict the corresponding model predictions.

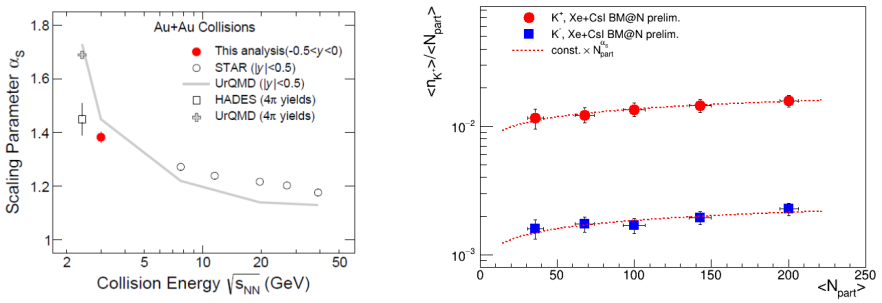


Figure 22: Left: Excitation function of the scaling parameter α_S for Au+Au collisions. The figure is taken from Ref. [3]. Right: The total multiplicity of $K^{\pm}$ scaled by the mean number of participants as a function of $\langle N_{part} \rangle$. The dashed lines depict the fits to $const. \cdot N_{part}^{\alpha_S}$ (see text for details).